Molecular Dynamics Simulation of Diffusion Behavior in Liquid Sn and Pb

MASATO SHIINOKI, AKIHIKO HIRATA, and SHINSUKE SUZUKI ⓘ

This study aimed to clarify the effect of a unique structure with a ''shoulder,'' which represents a hump on the high wave vector side of the first peak of static structure factor, in liquid Sn (liq-Sn) on the self-diffusion behavior through molecular dynamics (MD) simulation. The MD simulations of liq-Sn at 573 K and liquid Pb (liq-Pb) at 773 K were performed for comparison. The former and latter were selected as element with and without shoulder structure and reliable self-diffusion coefficients in liquid have been measured in both elements. The calculated self-diffusion coefficients of liq-Sn and liq-Pb were reproduced as the same order of magnitude with the referred reliable data of diffusion coefficients, which were obtained by experiments on the ground. The microscopic diffusion behavior of liq-Sn is unlike that of the hard-sphere model because the atoms become sluggish in the range that corresponds to the shoulder appearing in the pair distribution function of liq-Sn as well as in the structure factor of liq-Sn based on the local atomic configurations and time-series analyses of individual atoms. Therefore, the velocity autocorrelation function (VACF) converges to zero more rapidly than that of liq-Pb, and it is reproduced by the hard-sphere model. However, the macroscopic diffusion behavior of liq-Sn expressed by the self-diffusion coefficient is the same as that of the hard-sphere model with the non-correlation of the VACF in the long time.

I. INTRODUCTION

DIFFUSION coefficient in liquid metal is an essential thermophysical property for understanding metallurgical phenomena and modeling diffusion theories. For measuring the microscopic behavior and structure in the liquid metal, measurements using the quasi-elastic neutron scattering and X-ray scattering are effective, and they have already been reported by previous studies.[1–6] Especially, the polyvalent liquid metals like Sb, As, Bi, Ga, Ge, Si, and Sn have been reported for unique structures characterized by a shoulder which represents a hump on the high wave vector side of the first peak of static structure factor of these liquid metals.[7] This unique structure expresses as shoulder structure in this paper. The origin of the shoulder structures is still an unresolved issue in liquid metals that has been discussed not only experimentally but also by molecular dynamics (MD) simulation.[6,8,9] Several assumptions have been proposed to explain the physical cause of the shoulder structures; the explanations contain the a hard core with a ledge-shape repulsive,[10] the possibility of trapping particles in an energetically metastable position,[11] the interplay of two different scale lengths which are the effective hard-sphere diameter and the Friedel wave length,[9,12,13] the partial covalent bond structures affecting atoms from short and middle range order,[14–16] and the clusters primarily including tetrahedrons.[6,8,17] The liquid structures of these metals exhibit peculiar behaviors different from those of simple metallic liquids like Al and Pb, as represented by a shoulder.

In these anomalous metals, Sn is a kind of indispensable material industrially often used as a main element in solder. The fundamental physical properties of Sn are also unique. The solid Sn possesses two allotropes which

MASATO SHIINOKI is with the Institut für Materialphysik im Weltraum, Deutsches Zentrum für Luft- und Raumfahrt (DLR), Linder Höhe 51170 Köln, Germany and also with the Kagami Memorial Research Institute of Materials Science and Technology, Waseda University, Nishiwaseda 2-8-26 Shinjuku-ku, Tokyo 169-0051, Japan. Contact e-mail: Masato.Shiinoki@dlr.de AKIHIKO HIRATA is with the Kagami Memorial Research Institute of Materials Science and Technology, Waseda University and also with the Department of Materials Science, Graduate School of Fundamental Science and Engineering, Waseda University, Okubo 3-4-1 Shinjuku-ku, Tokyo 169-8555, Japan. SHINSUKE SUZUKI is with the Kagami Memorial Research Institute of Materials Science and Technology, Waseda University and also with the Department of Materials Science, Graduate School of Fundamental Science and Engineering, Waseda University and also with the Department of Applied Mechanics and Aerospace Engineering, Faculty of Science and Engineering, Waseda University, Okubo 3-4-1 Shinjuku-ku, Tokyo 169-8555, Japan.

are α-Sn and β-Sn.[18] At an ordinary temperature, the crystal of Sn has a tetragonal structure (β-Sn) above 286.4 K. Below 286.4 K its crystal structure changes of cubic structure (α-Sn). (α-Sn has the same tetrahedral diamond lattice as those of Si and Ge and shows a character of semiconductor. On the contrary, β-Sn has a metallic property. Itami et al. measured the structure factor of liquid Sn (liq-Sn) from 573 K to 1873 K using neutron scattering, and calculated the structure factor of the liq-Sn from the *ab initio* molecular dynamics (AIMD) simulation.[6] They reported that the shoulder in liq-Sn appears largely near the melting point and disappears with an increase in the temperature. Further, they proposed that the origin of the shoulder in liq-Sn would be the covalent bond in the short-range order based on the calculation of the angle distribution function. Moreover, to investigate the tetrahedral bond in liq-Sn, Zhao et al. measured the static structure factors of $In_{30}Sn_{70}$ from liquid 673 K to near solidus 398 K using X-ray diffraction.[15] They reported that the unusual features originating from the covalent bonding of Sn persist even in a liquid state. Zhang et al. also measured the static structure factors of InSn system along the liquidus based on the experimental results obtained using X-ray diffraction and discussed how the covalent bonding structures and viscosity change in the whole solidification process. Further more, they have suggested that when the melt is in the temperature range of 60 K above the liquidus, the melt retains more covalent bonding fragments originated from solid Sn. In addition, they also reported that increasing the coordination number or the population of covalent bonding in InSn liquid affects the static properties such as increasing viscosity.[16] However, there have been only a few studies that reported on the effect of a unique structure like a shoulder on dynamic behavior of self-diffusion in liquid metals.[19–22] The difficulty is development of a potential that can reproduce the unique structure, which makes it difficult to study the dynamics in detail owing to the high computational cost of the AIMD. With the rapid development of information science in recent years, the development of an interatomic potential that can be reproduced for the shoulder in liq-Sn has allowed us to perform large-scale MD simulations.[23]

Further, it is necessary to understand the microscopic behavior for discussing the contribution of the liquid structure to the diffusion mechanism. However, it is difficult to analyze the atomic behavior in the local structure in the liquid metal from scattering experiments. Therefore, this study focuses on MD simulation for analyzing the microscopic dynamic behavior of self-diffusion in liq-Sn. It is useful to use MD simulation to analyze the microscopic behavior of self-diffusion in the liquid metal.[24–30] Especially, one indicator of the dynamic properties in liquid metal is a velocity autocorrelation function (VACF) that represents the microscopic dynamic behavior of an atom. Alder et al. calculated the VACF by the MD simulation for 108 or 500 particles using a hard-sphere potential.[24] The high-density VACF becomes negative in the middle, which means that when one atom is moving in a certain direction, another atom is more likely to be moving in

the opposite direction. This indicates the presence of strong interactions which include collisions as well as interatomic forces between atoms in the system. This calculation result from MD simulation revealed that the high-density state promotes the irregular motion of atoms, which expresses the negative value of the VACF and is also called as backscattering. Especially, Calderín et al. calculated the VACF of liq-Sn from AIMD simulation using 205 atoms at simulation temperatures of 573 and 1273 K.[26] They reported that the VACF of liq-Sn exhibits the negative value with a first minimum which is not so deep as in liquid Pb (liq-Pb) but much deeper that in liquid Si. This behavior was connected to the cage effect,[31] that is, whereas the loose packed structure of liquid Si induced a very weak backscattering, the closed packed structure of liq-Pb yielded a stronger backscattering and a deeper first minimum. To understand the microscopic behavior of VACF in more detail, it is necessary to link it to the microscopic behavior of liquid structures on an atomic scale and time-series analysis of atomic trajectories.

Therefore, this study aims to clarify the effect of the shoulder in liq-Sn on the self-diffusion behavior through MD simulation. The selected elements for the MD simulation were Sn and Pb. Sn was selected as a representative element with a shoulder. Pb was selected as the representative element that reproduces a hard-sphere model and a closed packed liquid for comparison of the effect of the shoulder on microscopic and macroscopic diffusion behaviors. In addition, reliable self-diffusion coefficients in liq-Sn and liq-Pb have been measured under microgravity conditions[32,33] and our previous ground-based experiments.[34,35] The macroscopic diffusion behavior was evaluated for correctness using the self-diffusion coefficient of Sn and Pb obtained from experiments to determine the validity of the MD calculation. The VACF in each element was calculated for analyzing dynamic properties in a short-time range. The local structure and time series of these elements were analyzed for coordination atoms up to the second nearest neighbor. Further, the time series of the atomic motion in the local configuration was calculated.

II. COMPUTATIONAL METHODOLOGY

The MD simulation was conducted using the LAMMPS package (19 Sep 2019 version).[36] The modified embedded-atom force field was used for the pair potential of Sn,[23] and the embedded-atom force field was used for the pair potential of Pb.[37] A total of 4096 atoms with the body-centered tetragonal structure (lattice constant in a-axis: $a = 5.83$ Å and in c-axis: $c = 3.18$ Å)[38] and 4000 atoms with the face centered cubic structure ($a = 4.94$ Å)[39] arranged in a cubic simulation box with periodic boundary conditions were considered for the MD simulation of Sn and Pb, respectively. Each atom is given a serial number (ID). The MD simulations were conducted by integrating Newton's equations of motion using the velocity-Verlet algorithm with a time step of 1.0 fs. Targeted temperatures of Sn and Pb were 573 K and 773 K, respectively; these temperatures were

decided by the same conditions as the reference self-diffusion measurements upon melting points of Sn and Pb under microgravity conditions[32,33] and our previous ground-based experiments.[34,35] Further, the targeted temperature of Sn was selected so as to be near the melting point at which the shoulder is expressed. The lengths of one side of the cubic simulation box of Sn and Pb were 48.96 Å and 51.69 Å, respectively. They were decided from the volumes of the cubic simulation box after relaxing that box at the atmospheric pressure using an isothermal-isobaric ensemble for each targeted temperature. The visualizations of the atoms were obtained using OVITO, which is a scientific visualization and analysis software for atomic and particle simulation data.[40] Before performing the targeted calculation, the thermal equilibrium process is implemented on simulation box as follows. First, the liquid sample was simulated at 2000 K during 3 ps using a canonical (NVT) ensemble by means of a Nosé–Hoover thermostat to control temperature. Second, the simulation box was cooled from 2000 K to the targeted temperature and equilibrated at the targeted temperature during 18 ps using the NVT ensemble. After the thermal equilibrium process, the targeted calculation was run during 100 ps using NVT ensemble, and then, the time-series data of the atomic position were obtained. The output was obtained at every $\Delta t = 0.1$ ps. The pair distribution functions $g(r)$ of Sn and Pb were calculated from histogram of atoms by normalization using the following equation.

$$g(r) = \frac{n(r)}{4\pi r^2 \Delta r \rho} \qquad [1]$$

Here ρ, $\Delta r = 0.02$ Å, and $n(r)$ represent the number density, a radial bin, and the number of atoms at a distance in a range between r and $r + \Delta r$ from a center atom, respectively. The $g(r)$ was calculated with each atom as the center, and the average of $g(r)$ among all atoms was used. The structure factors $S(Q)$ also were calculated from the results of $g(r)$ using the following equation, which is connected by the Fourier transform relationship.

$$S(Q) = 1 + 4\pi\rho \int_0^\infty r^2 (g(r) - 1) \frac{sin(Qr)}{Qr} dr \qquad [2]$$

Here Q represents wave vector. The integral range of dr was set to a half of the simulation box length. The position data of Sn and Pb when starting the targeted calculations were used.

III. RESULTS

Figure 1 shows the calculated $S(Q)$ of Sn and Pb with the experimental data of liq-Sn[7] and liq-Pb[7] obtained from the X-ray scattering experiments and the calculated data from AIMD.[26] The results included not only the experimental data but also the AIMD data because the experimental data alone would not be sufficient to verify our results. Oscillations were observed throughout both of $S(Q)$, especially around low Q values. These were
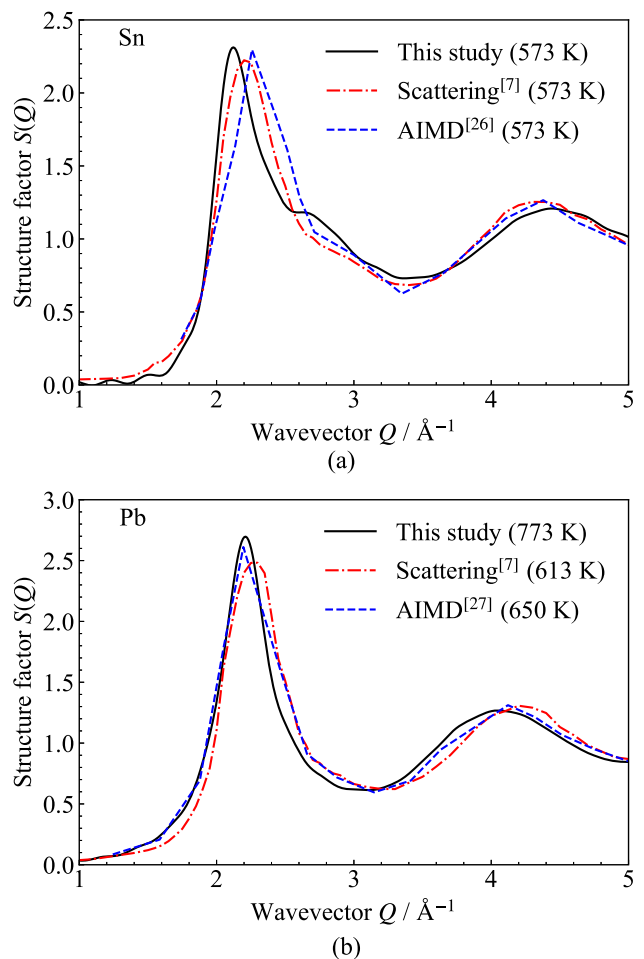

Fig. 1—Calculated structure factors: (a) liquid Sn at 573 K and (b) liquid Pb at 773 K. Scattering and AIMD indicates the data from X-ray scattering measurement and ab initio molecular dynamics simulation, respectively.

unphysical errors introduced during the Fourier transform. The $S(Q)$ of Sn had a first peak at 2.1 Å^{-1} and changed the curve gradient discontinuously from 2.5 to 3.5 Å^{-1}. This range agreed with the start to end of a shoulder referred to the experiment and the AIMD simulation. Therefore, the shoulder around 2.5 to 3.5 Å^{-1} was well reproduced for the structure factor of liq-Sn at 573 K as reported in a previous work.[6] The $S(Q)$ of Pb had a first peak at 2.2 Å^{-1} and a continuous curve from 2.5 to 3.5 Å^{-1} compared to the $S(Q)$ of Sn. Although the first peaks of both $S(Q)$ were slightly lower than the those of experiments, the states of both liq-Sn and liq-Pb were well reproduced at the beginning of the calculation because the presence or absence of a shoulder was reproduced.

The mean-square diffusion depths (MSD) were calculated from the time-series data of all positions of Sn and Pb; the self-diffusion coefficients of Sn and Pb in the simulation box were obtained. The MSD and self-diffusion coefficient D are defined as

$$MSD(t) = \frac{1}{N}\sum_{i=1}^{N}|x_i(t) - x_i(0)|^2 \qquad [3]$$

$$D = \lim_{t \to \infty} \frac{MSD(t)}{6t} \qquad [4]$$

where N, i, $\boldsymbol{x}_i$, and t represent the number of all atoms in the simulation box, number from the small order of the ID of atoms, position vector, and calculation time. Figure 2 shows the calculated self-diffusion coefficients of Sn and Pb. In experimental data about self-diffusion coefficients, the experiments conducted under the microgravity conditions would be reliable because self-diffusion coefficients can be measured with high accuracy due to the absence of buoyancy-driven convention. On the other hand, the experiments conducted on the ground used our data and the suppression of buoyancy-driven convections on the ground has been verified in our papers.[34,35] Both of self-diffusion coefficients provided high immediately after the start of the calculation, decreased with calculation time, and then remained constant with some variance. The values of the self-diffusion coefficients of Sn and Pb at 100 ps when the calculation finished were 2.29×10^{-9} and 2.56×10^{-9} $m^2 s^{-1}$, respectively. These self-diffusion coefficients have lower values than those obtained under microgravity conditions,[32,33] on the ground,[34,35] and from AIMD.[26] However, because the differences between the results of the experiments and the results from the calculations of Sn and Pb were not out of the order of magnitude, these
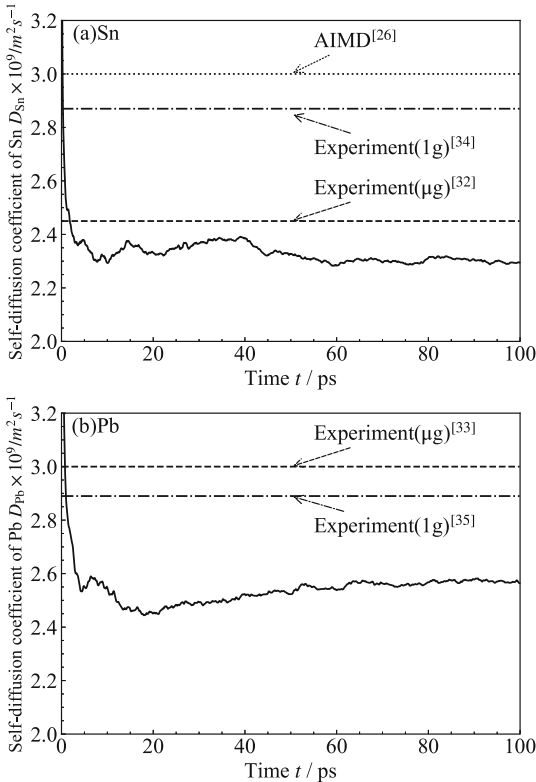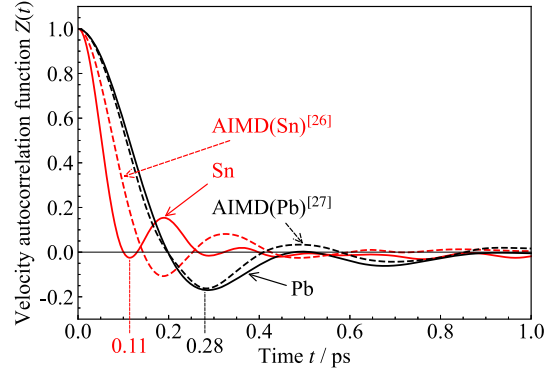

Fig. 3—Calculated velocity autocorrelation functions of Sn and Pb. AIMD indicates the data from *ab initio* molecular dynamics simulation.

calculations were considered as those reproduced by the above experimental results.

$$Z(t) = \frac{1}{N} \sum_i^N \frac{\boldsymbol{v}_i(t) \cdot \boldsymbol{v}_i(0)}{\boldsymbol{v}_i(0) \cdot \boldsymbol{v}_i(0)} \qquad [5]$$

where $\boldsymbol{v}$ denotes the velocity vector of an atom, and the dot refers to the inner product. Figure 3 shows the calculated VACF of Sn and Pb. The VACF of Sn had a minimum at 0.11 ps with $Z(t) \approx 0$, and it converged to 0 after an oscillation of $Z(t) > 0$. Like the hard-sphere model, the VACF of Pb showed a convergence behavior similar to 0 after passing through the region $Z(t) < 0$. The value of $Z(t)$ of Pb at the first minimum was deeper than that of Sn, which was the same tendency of the previous research.[26] Therefore, the VACF of the liquid Sn showed a microscopic behavior with a minimum value at 0.11 ps with $Z(t) \approx 0$ unlike the hard-sphere model. As time passed, $Z(t)$ became zero for both Sn and Pb.

IV. DISCUSSION

Local structure analysis using the pair distribution function and time series analyses of the individual atoms were performed for coordination atoms up to the second nearest neighbor. This aimed to investigate the relationship between the diffusion of atoms and the liquid structure with the shoulder, which appears in the pair distribution function as well as in the structure factor. The local structures of liq-Sn and liq-Pb were visualized, and the coordination atoms of Sn were compared to that of Pb. Finally, the influence of atoms at the shoulder region in the pair distribution function on the microscopic dynamic behavior of Sn was discussed in terms of the relationship between the VACF and the configuration atoms.

A. *Local Atomic Configurations up to the Second Nearest Neighbor*

The pair distribution functions $g(r)$ of Sn and Pb were calculated from not only the position data starting at the targeted calculation but also the initial crystal structure. Figures 4 and 5 shows the calculated pair distribution

Fig. 2—Calculated self-diffusion coefficients: (*a*) liquid Sn at 573 K and (*b*) liquid Pb at 773 K. Experiment (1g), Experiment (μg), and AIMD indicate the data from self-diffusion measurement on the ground, measurement under the microgravity condition, and *ab initio* molecular dynamics simulation, respectively.
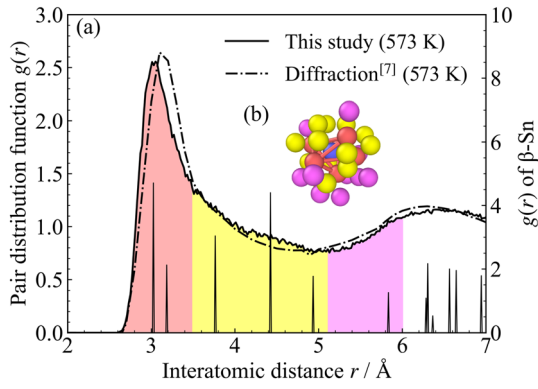
Fig. 4—(a) Calculated pair distribution function $g(r)$ of liq-Sn at 573 K and (b) visualization of typical local atomic configurations up to 6 Å. Each color area in (a) corresponds to the position of atoms from the center of the blue atom in (b). Red bars in (b) indicate bonds between a pair of red atoms. The vertical line expresses the $g(r)$ of β-Sn (Color figure online).
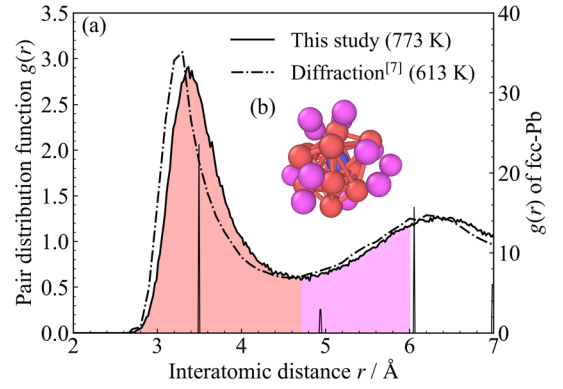

Fig. 5—(a) Calculated pair distribution function $g(r)$ of liq-Pb at 773 K and (b) visualization of typical local atomic configurations up to 6 Å. Each color area in (a) corresponds to the position of atoms from the center of the blue atom in (b). Red bars in (b) indicate bonds between a pair of red atoms. The vertical line expresses the $g(r)$ of fcc-Pb (Color figure online).

functions of l- and β-Sn, and l- and solid Pb (fcc-Pb), respectively, together with the local atomic configurations. As shown in Figure 4(a), the nearest neighbor atoms up to the interatomic distance $r = 3.5$ Å [atoms shown in red color in Figure 4(b)] and next neighbor atoms from 5.1 to 6.0 Å [atoms shown in violet color in Figure 4(b)] were defined. As shown in Figure 4(a), the next nearest neighbor atoms [atoms shown in yellow color in Figure 4(b)] can be viewed at a shoulder of $g(r)$, which represents a hump on the high interatomic distance side of the first peak of $g(r)$, from 3.5 to 5.1 Å corresponding to the start to the end of the discontinuity in the curve gradient. Therefore, the pair distribution function of liq-Sn has a liquid structure with a shoulder in real space as well as the structure factor of liq-Sn. As shown in Figure 5(a), the nearest neighbor atoms up to 4.7 Å which was the first minimum to the right of the first peak of $g(r)$ [atoms shown in red color in Figure 5(b)] and the next neighbor atoms from 4.7 to 6.0 Å [atoms shown in violet color in Figure 5(b)] were defined. The ranges of coloring corresponded roughly to the positions of the neighboring atoms in β-Sn and fcc-Pb, respectively. The coordination numbers were calculated using the method[7] of minimum value as following this equation.

$$N_{cood} = \int_0^{r_m} 4\pi\rho r^2 g(r) dr \qquad [6]$$

Here N_{cood} and r_m represent the coordination number and the interatomic distance of the maximum value of integration in the $4\pi\rho r^2 g(r)$ curve. N_{cood} of liq-Sn had 5.9 in the nearest neighbor atoms up to $r_m = 3.5$ Å and 18.3 in the next nearest neighbor atoms up to $r_m = 5.1$ Å which was the first minimum to the right of the first peak of $4\pi\rho r^2 g(r)$ curve with the shoulder of $g(r)$. On the other hand, N_{cood} of β-Sn had 6 up to $r_m = 3.5$ (second nearest neighbor) and 18 up

to $r_m = 4.4$ Å (fourth nearest neighbor). Comparing N_{cood} of liq-Sn with that of β-Sn, the atoms of Sn located in the range corresponding to the shoulder of $g(r)$ corresponded to third and fourth nearest neighbors in β-Sn. N_{cood} of liq-Pb had 12.3 in the nearest neighbor atoms up to $r_m = 4.7$ Å. That was almost the same corresponding to the N_{cood} of fcc-Pb (12 atoms) to the nearest neighbor. Therefore, the local atomic configurations of the nearest neighbor atoms, which include the shoulder of $g(r)$ in the liq-Sn, were cleared to have a higher coordination number in Sn than that in Pb.

Further, the angle distribution functions $g^{(3)}(\theta, r_c)$ of Sn and Pb were calculated to determine how the surrounding atoms were distributed spatially. Figures 6 and 7 show the calculated angle distribution functions of liq- and β-Sn, and liq- and fcc-Pb, respectively, together with the visualization of the local atomic configurations in a plane with a thickness of 3.2 Å. The bond angle θ is defined by a pair of vectors drawn from a reference atom to any other two atoms within the sphere of the cutoff radius r_c. This calculation was performed by the following procedure: (i) select the central atom, (ii) calculate the direction vectors from the central atom to two pickup atoms within r_c, and (iii) calculate the angle between the two vectors from each inner product divided the product of the norms. The area of $g^{(3)}(\theta, r_c)$ is normalized to 1. As shown in Figure 6, the nearest neighbor atoms in liq-Sn at less than $r_c = 3.3$ Å remained the directivity of the covalent bonds around 109° originated from β-Sn within the second nearest neighbor. However, the atoms become sluggish in the range corresponding to the shoulder of $g(r)$ in liq-Sn disappeared the directivity of the covalent bonds at r_c less than 4.7 Å because of the complex distribution surround the atomic configurations in β-Sn within fourth nearest neighbor. On the other hand, as shown in Figure 7, the nearest neighbor atoms in liq-Pb at r_c in
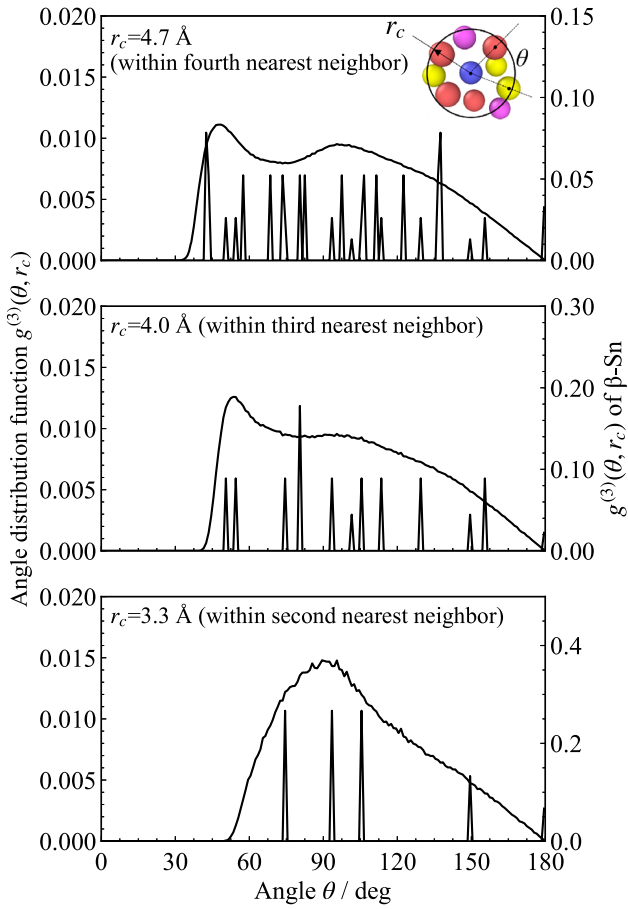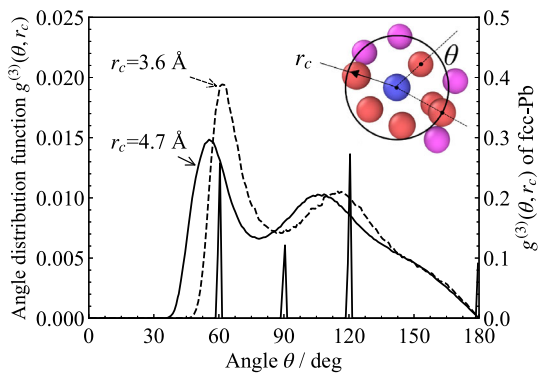
Fig. 6—Calculated angle distribution function $g^{(3)}(\theta, r_c)$ of liq-Sn at 573 K. The visualization of the local atomic configurations includes in a plane with a thickness of 3.2 Å. The bond angle θ is defined by a pair of vectors drawn from a reference atom to any other two atoms within the sphere of the cutoff radius r_c. Each color atom corresponds to the position of atoms from the center of the blue atom in Fig. 4. The vertical line expresses the $g^{(3)}(\theta, r_c)$ of β-Sn (bct-Sn) and each nearest neighbor means the coordination in β-Sn (Color figure online).

Fig. 7—Calculated angle distribution function $g^{(3)}(\theta, r_c)$ of liq-Pb at 773 K. The visualization of the local atomic configurations includes in a plane with a thickness of 3.2 Å. The bond angle θ is defined by a pair of vectors drawn from a reference atom to any other two atoms within the sphere of the cutoff radius r_c. Each color atom corresponds to the position of atoms from the center of the blue atom in Fig. 5. The vertical line expresses the $g^{(3)}(\theta, r_c)$ of fcc-Pb within the first nearest neighbor (Color figure online).

the range from 3.6 to 4.7 Å had peaks around 60° and 120°, which indicates a dependence of the bond angle between atoms in liq-Pb as the same directivity as that in fcc-Pb. The parallel shift of the $g^{(3)}(\theta, r_c)$ of liq-Pb to the with increasing r_c was due to the increasing influence of the atoms in the second nearest neighbor. That is, the probability of finding the atoms of Sn was more uniformly distributed than that of Pb; therefore, an atomic configuration within the shoulder of $g(r)$ in the liq-Sn was cleared to be more dispersed in the surroundings than that of liq-Pb.

B. Time-Series Analyses of Individual Atoms

The time-series behavior of coordination atoms was analyzed by focusing on individual atoms and displaying the surrounding coordination atoms. Figure 8 shows examples of the calculated time-series behaviors of the coordination atoms of Sn and Pb. Each color shown in Figure 8 corresponds to the color defined in the range of the pair distribution function of Sn and Pb in Figures 4 and 5. The calculation process of this analysis is shown below:

1) An atom called the central atom is focused.
2) Atoms that exist within the sphere of the cutoff radius r_c are calculated for the surrounding atoms.
3) After a lapse of Δt, the positions of atoms within r_c were calculated again, and the distance from the central atom was displayed, as indicated in Figure 8. Further, as shown in Figures 8(a) and (b), the configuration atoms of Sn from the central atom, which is ID450, were within the range 3.5–5.1 Å and they corresponded to the shoulder of $g(r)$. In addition, as shown in Figures 8(c) and (d), the configuration atoms of Pb from the central atom, which is ID857, moved back and forth between the nearest neighbor and next nearest neighbor. Thus, it was cleared that atoms at the shoulder of $g(r)$ in the liq-Sn could stay longer than those in Pb in the time series.

Some MSDs for individual Sn atoms were calculated to analyze the microscopic behavior of the self-diffusion of Sn. Figure 9 shows examples of MSDs for the individual atoms of Sn and Pb and for all atoms from 0 to 10 ps. The MSDs for the ID450 and ID857 atoms were abnormally larger than those for the ID451 and the ID210 atoms shown in Figures 9(a) and (b), respectively. The behaviors of the rapid increase in both MSDs for the ID450 atom of Sn around 2 ps and for the ID857 atom of Pb around 7 ps were confirmed. This behavior of the rapid increase in the MSD can be attributed to jump diffusion, and this has been reported in a previous work related to the MD simulation of the liquid Ar.[24] Thus, the existence of jump diffusion was confirmed in both the liq-Sn and liq-Pb. However, the relationship between the jump diffusion and the shoulder of $g(r)$ in the liq-Sn remains unclear because the analysis in this study did not reveal any difference in the local atomic motion of Sn and Pb in the space where the jump occurred.
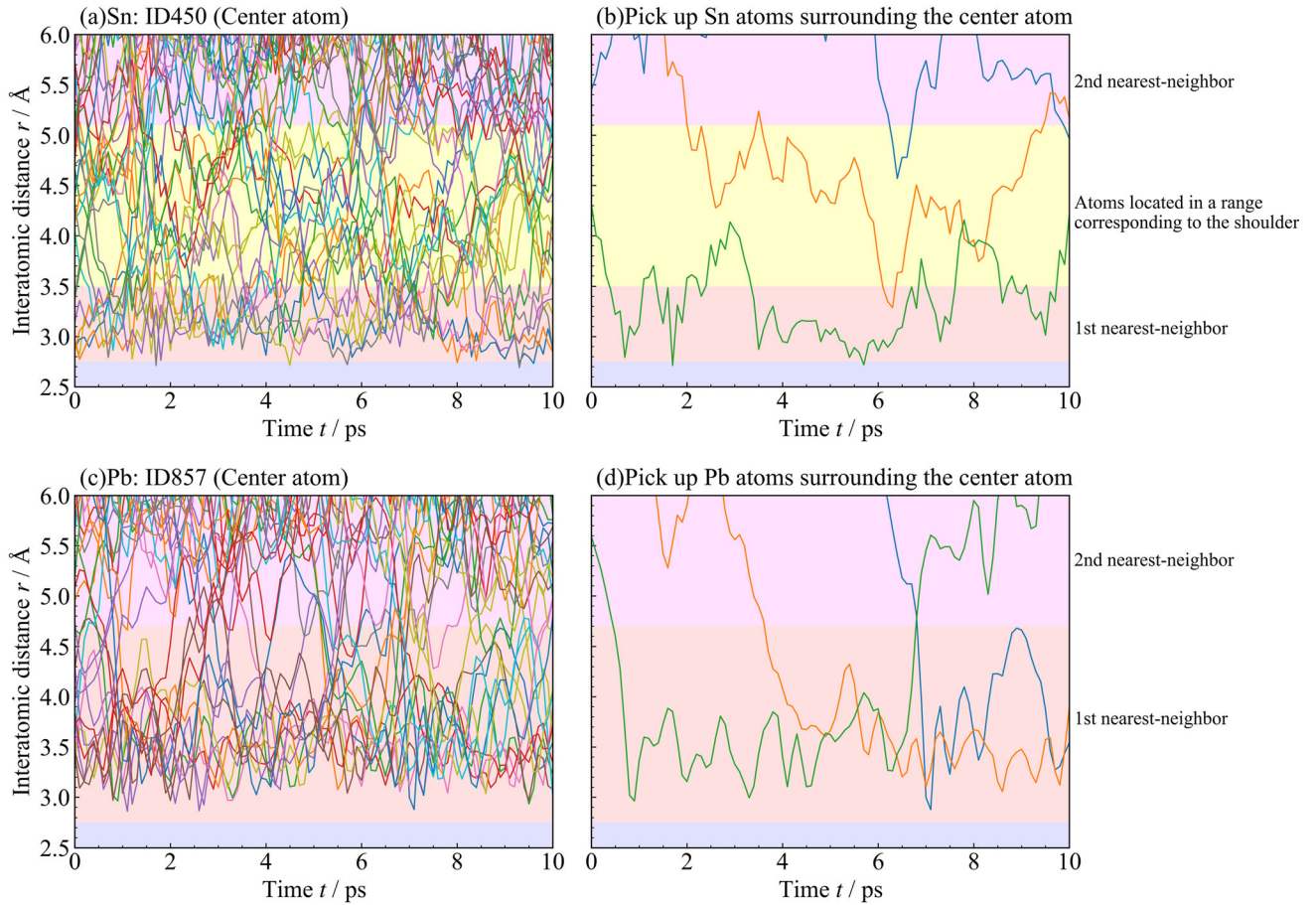
Fig. 8—Examples of calculated time-series behaviors of coordination atoms: (*a*) liq-Sn at 573 K from the central atom ID450, (*b*) three atoms were pick up from (a), (*c*) liq-Pb at 773 K from the central atom ID857, and (*d*) three atoms were pick up from (c). Each color area corresponds to the position of atoms from the center of the blue atom in Figs. 4 and 5 (Color figure online).

C. *Effect of the Shoulder in Liquid Sn on the Self-diffusion Behavior*

The above discussions suggest that the effect of the shoulder in the liq-Sn on the self-diffusion behavior can be considered as follows: As shown in Figure 4, the pair distribution function of liq-Sn has a liquid structure with a shoulder as well as the structure factor. The atomic motion of Sn is inhibited by the surrounded atoms owing to the presence of the atoms in the range that correspond to the shoulder of $g(r)$ closer to the central atom. Further, atoms of Sn in the range that correspond to the shoulder of $g(r)$ in liq-Sn can stay in the time series and atoms of Pb cannot stay long between the first and second peak of $g(r)$ in liq-Pb because of no shoulder of $g(r)$ in liq-Pb. Thus, when the central atom of Sn diffuses, that is, it is blocked by the surrounding atoms in the range corresponding to the shoulder of $g(r)$, the VACF of Sn is considered to converge rapidly to zero as shown in Figure 3. This indicates that atoms of Sn become sluggish in the range corresponding to the shoulder of $g(r)$, which causes a sudden decrease in the VACF to the negatively large value. This tendency is different from the behavior of the hard-sphere model. The shoulder will not have a significant effect on the macroscopic diffusion behavior because the VACF becomes zero over time, for both Sn and Pb.

V. CONCLUSIONS

The diffusion behavior in the liquid Sn and Pb was analyzed using MD simulation. The calculated self-diffusion coefficients of Sn and Pb were reproduced in the same order of magnitude with the referred reliable data of diffusion coefficients, which were obtained by experiments on the ground. The velocity autocorrelation function of Sn reached a minimum value close to zero at 0.11 ps.

Based on the local atomic configurations and time-series analyses of individual atoms obtained by MD simulation, the next nearest neighbor atoms can be seen in a shoulder appearing in the pair distribution function of liquid Sn. The atomic motion of Sn is inhibited by the atoms around the next nearest neighbor sites when the diffusion of Sn atoms occurs. This is because the first nearest neighbor atoms are located closer to the atoms in the range corresponding to the shoulder than the
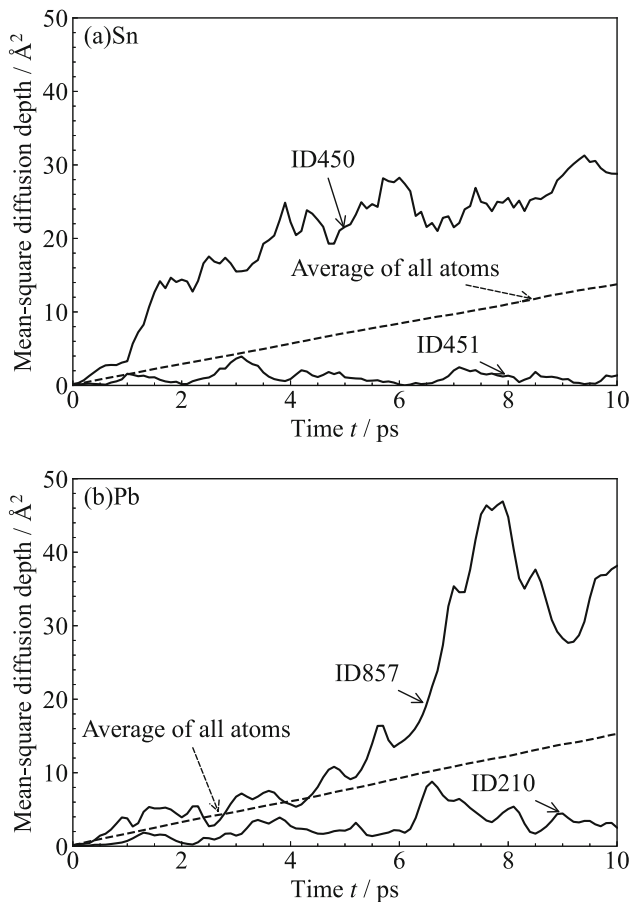
Fig. 9—Examples of mean-square diffusion depth (MSD): (*a*) individual Sn atoms at 573 K and (*b*) individual Pb atoms at 773 K.

NOMENCLATURE

a	Lattice constant in a-axis (Å)
c	Lattice constant in c-axis (Å)
D	Self-diffusion coefficient ($m^2\ s^{-1}$)
$g(r)$	Pair distribution function
$g^{(3)}(\theta, r_c)$	Angle distribution function
ID	Serial number of atoms
MSD	Mean-square diffusion depth ($Å^2$)
N	Number of all atoms in a simulation box
N_{cood}	Coordination number
$n(r)$	Number of atoms at a distance between r and $r + \Delta r$ from a center atom
Q	Wave vector ($Å^{-1}$)
Δr	Radial bin (Å)
r	Interatomic distance (Å)
r_c	Cutoff radius (Å)
r_m	Interatomic distance of the Maximum value of $4\pi\rho r^2 g(r)$ curve (Å)
$S(Q)$	Structure factor
t	Time (ps)
Δt	Output interval time (ps)
$\boldsymbol{v}$	Velocity vector of an atom ($m\ s^{-1}$)
$\boldsymbol{x}$	Position vector (m)
$Z(t)$	Velocity autocorrelation function

GREEK SYMBOLS

θ	Bond angle (deg)
ρ	Number density (atoms $Å^{-3}$)

SUBSCRIPTS

i	Number from the small order of the ID of atoms

central atom. Therefore, the velocity autocorrelation function of Sn is considered to converge rapidly to zero. This suggests that the microscopic dynamic behavior of Sn is different from the behavior of the hard-sphere model. In addition, the shoulder does not have a significant effect on the macroscopic diffusion behavior because the VACF became zero over time.

CONFLICT OF INTEREST

On behalf of all authors, the corresponding author states that there is no conflict of interest.

OPEN ACCESS

REFERENCES

1. A. Meyer, L. Hennig, F. Kargl, and T. Unruh: *J. Phys. Condens. Matter*, 2019, vol. 31, p. 395401.
2. S. Hosokawa, J. Greif, F. Demmel, and W.-C. Pilgrim: *Chem. Phys.*, 2003, vol. 292, pp. 253–61.
3. U. Dahlborg, M. Besser, M. Calvo-Dahlborg, S. Janssen, F. Juranyi, M.J. Kramer, J.R. Morris, and D.J. Sordelet: *J. Non-Cryst. Solids*, 2007, vol. 353, pp. 3295–99.
4. S. Hosokawa, W.-C. Pilgrim, and F. Demmel: *J. Non Cryst. Solids*, 2007, vol. 353, pp. 3122–28.
5. F. Demmel: *J. Phys. Condens. Matter*, 2018, vol. 30, p. 495102.
6. T. Itami, S. Munejiri, T. Masaki, H. Aoki, Y. Ishii, T. Kamiyama, Y. Senda, F. Shimojo, and K. Hoshino: *Phys. Rev. B*, 2003, vol. 67, p. 064201.
7. Y. Waseda: *The Structure of Non-Crystalline Materials: Liquids and Amorphous Solids*, McGraw-Hill International Book Company, 1980.
8. V. Petkov and G. Yunchov: *J. Phys. Condens. Matter*, 1994, vol. 6, p. 10885.
9. K.H. Tsai, T.-M. Wu, and S.-F. Tsay: *J. Chem. Phys.*, 2010, vol. 132, p. 034502.
10. M. Silbert and W.H. Young: *Phys. Lett. A*, 1976, vol. 58, pp. 469–70.
11. K.K. Mon, N.W. Ashcroft, and G.V. Chester: *Phys. Rev. B Condens. Matter*, 1979, vol. 19, pp. 5103–22.
12. J. Hafner and G. Kahl: *J. Phys. F*, 1984, vol. 14, p. 2259.
13. J. Hafner and W. Jank: *Phys. Rev. B*, 1990, vol. 42, pp. 11530–39.
14. X.G. Gong, G.L. Chiarotti, M. Parrinello, and E. Tosatti: *EPL*, 1993, vol. 21, p. 469.
15. Y. Zhao, X. Bian, X. Qin, J. Qin, and X. Hou: *Phys. Lett. A*, 2006, vol. 356, pp. 385–91.
16. K. Zhang, X. Bian, L. Yang, and Y. Bai: *Physica B*, 2012, vol. 407, pp. 2141–45.
17. L.-Y. Chen, P.-H. Tang, and T.-M. Wu: *J. Chem. Phys.*, 2016, vol. 145, p. 024506.
18. R. Pöttgen: *Z. Nat. B*, 2006, vol. 61, pp. 677–98.
19. H. Weis, D. Holland-Moritz, F. Kargl, F. Yang, T. Unruh, T.C. Hansen, J. Bednarčik, and A. Meyer: *Phys. Rev. B*, 2021, vol. 104, p. 134108.
20. K. Kimura, K. Matsuda, T. Nagao, T. Hagiya, Y. Kajihara, M. Inui, J. Nakamura, A. Chiba, K. Hayashi, M. Itou, and Y. Sakurai: *J. Phys. Soc. Jpn.*, 2017, vol. 86, p. 124703.
21. Y. Kawakita, T. Kikuchi, Y. Inamura, S. Tahara, K. Maruyama, T. Hanashima, M. Nakamura, R. Kiyanagi, Y. Yamauchi, K. Chiba, S. Ohira-Kawamura, Y. Sakaguchi, H. Shimakura, R. Takahashi, and K. Nakajima: *Physica B*, 2018, vol. 551, pp. 291–96.
22. Q. Sun, J. Qin, X. Li, J. Wang, and S. Pan: *J. Phase Equilib. Diffus.*, 2021, vol. 42, pp. 166–74.
23. J.R. Vella, M. Chen, F.H. Stillinger, E.A. Carter, P.G. Debenedetti, and A.Z. Panagiotopoulos: *Phys. Rev. B*, 2017, vol. 95, p. 064202.
24. B.J. Alder, D.M. Gass, and T.E. Wainwright: *J. Chem. Phys.*, 1970, vol. 53, p. 3813.
25. M. Tanaka, H. Fukui, and S. Takeuchi: *J. Japan Inst*, 1973, vol. 37, pp. 907–16.
26. L. Calderín, D.J. González, L.E. González, and J.M. López: *J. Chem. Phys.*, 2008, vol. 129, p. 194506.
27. M.M.G. Alemany, R.C. Longo, L.J. Gallego, D.J. González, L.E. González, M.L. Tiago, and J.R. Chelikowsky: *Phys. Rev. B*, 2007, vol. 76, p. 214203.
28. A. Meyer, J. Horbach, O. Heinen, D. Holland-Moritz, and T. Unruh: *Defect Diffus. For.*, 2009, vol. 289–292, pp. 609–14.
29. J. Qin, X. Li, J. Wang, and S. Pan: *AIP Adv.*, 2019, vol. 9, p. 035328.
30. B.G. del Rio, C. Pascual, L.E. González, and D.J. González: *J. Phys. Condens. Matter*, 2020, vol. 32, p. 214005.
31. J.-P. Hansen and I.R. McDonald: *Theory of Simple Liquids: With Applications to Soft Matter*, 4th ed. Academic Press, San Diego, CA, 2013.
32. Y. Malmejac and G. Frohberg: in *Fluid Sciences and Materials Science in Space: A European Perspective*, H.U. Walter, ed., Springer Berlin Heidelberg, Berlin, Heidelberg, 1987, pp. 159–90.
33. G. Mathiak, A. Griesche, K.H. Kraatz, and G. Frohberg: *J. Non Cryst. Solids*, 1996, vol. 205–207, pp. 412–16.
34. M. Shiinoki, N. Hashimoto, H. Fukuda, Y. Ando, and S. Suzuki: *Metall. Mater. Trans. B*, 2018, vol. 49B, pp. 3357–66.
35. M. Shiinoki, Y. Nishimura, K. Noboribayashi, and S. Suzuki: *Metall. Mater. Trans. B*, 2021, vol. 52B, pp. 3846–59.
36. S. Plimpton: *J. Comput. Phys.*, 1995, vol. 117, pp. 1–9.
37. K. Wang, W. Zhu, M. Xiang, Y. Xu, G. Li, and J. Chen: *Modell. Simul. Mater. Sci. Eng.*, 2018, vol. 27, p. 015001.
38. V.T. Deshpande and D.B. Sirdeshmukh: *Acta Crystallogr.*, 1961, vol. 14, pp. 355–56.
39. M.E. Straumanis: *J. Appl. Phys.*, 1949, vol. 20, pp. 726–34.
40. A. Stukowski: *Model. Simul. Mater. Sci. Eng.*, 2010, vol. 18, p. 015012.